LAWRENCE
LIVERMORE
NATIONAL
LABORATORY

LLNL-JRNL-677081

High-power Laser Interaction With Low-density C-Cu Foams

F. Perez, J. D. Colvin, M. J. May, S. Charnvanichborikarn, S. O. Kucheyev, T. E. Felter, K. B. Fournier

September 11, 2015

Physics of Plasmas

Disclaimer

This document was prepared as an account of work sponsored by an agency of the United States government. Neither the United States government nor Lawrence Livermore National Security, LLC, nor any of their employees makes any warranty, expressed or implied, or assumes any legal liability or responsibility for the accuracy, completeness, or usefulness of any information, apparatus, product, or process disclosed, or represents that its use would not infringe privately owned rights. Reference herein to any specific commercial product, process, or service by trade name, trademark, manufacturer, or otherwise does not necessarily constitute or imply its endorsement, recommendation, or favoring by the United States government or Lawrence Livermore National Security, LLC. The views and opinions of authors expressed herein do not necessarily state or reflect those of the United States government or Lawrence Livermore National Security, LLC, and shall not be used for advertising or product endorsement purposes.

High-power laser interaction with low-density C–Cu foams

F. Pérez,[1, a)] J. D. Colvin,[1] M. J. May,[1] S. Charnvanichborikarn,[1] S. O. Kucheyev,[1] T. E. Felter,[2] and K. B. Fournier[1, b)]

[1)] *Lawrence Livermore National Laboratory, 7000 East Ave., Livermore CA 94550 USA*

[2)] *Sandia National Laboratories, 7011 East Ave., Livermore, CA 94550 USA*

We study the propagation of high-power laser beams in micro-structured carbon foams by monitoring the x-ray output from deliberately introduced Cu content. In particular, we characterize this phenomenon measuring absolute time-resolved x-ray yields, time-resolved x-ray imaging, and x-ray spectroscopy. New experimental results for C–Cu foams show a faster heat front velocity than simulation that assumed homogeneous plasma. We suggest the foam micro-structure may explain this trend.

I. INTRODUCTION

Micro- or nano-structured materials are becoming targets of choice in many laser-plasma interaction studies. For example, with short-pulse lasers, foams can provide additional electron acceleration[1], and nano-wires can enhance the x-ray generation[2]. With long-pulse lasers, foams may increase the efficiency of holhraums[3]. In the field of multi-keV-x-ray generation by high-power laser-plasma interaction, foam targets have also proven great potential[4–6], competing with metal foils[7], pre-exploded foils[8] or gas-filled targets[9–11]. The best laser-to-multi-keV-x-ray conversion efficiencies of these various types of targets vary between 0.5 and 15%, depending on the atomic number of the emitters.

In our effort to develop bright x-ray sources spanning a large range of photon energies we investigate, in this article, the x-ray output of Cu-loaded foam targets. The x-ray energy range of interest corresponds to the Cu K-shell transitions from 8 to 10 keV. In addition to measuring the x-ray yield and content, one key element to understand and predict accurately the laser-foam interaction is the propagation velocity of the laser and of its associated heat front. When the foam average electron density is lower than the critical density[12] n_c, the laser tends to propagate over long distances (millimeters). It is thus able to heat uniformly a large volume of plasma, generating, in turn, copious amounts of x rays. The heat front velocity characterizes the evolution of the interaction volume and, as such, relates to the total heated volume and to the peak temperature. Consequently, it offers important insight into the x-ray generation.

Previous work using foam targets[13,14] has shown that the experimental measurements of the heat front velocity are not reproduced correctly by state-of-the-art simulations: the heat front is up to twice slower in experiments than in simulations. This discrepancy is generally assumed to be related to the micro-structure of the foams[15], which is not accounted for in simulations. The resolution of the numerical models does not allow for a proper representation of the small-scale filaments and voids composing the foam, which is assumed uniform instead. In the present article, we show new experimental results on Cu-loaded foams, revealing the opposite discrepancy with the same numerical code: the heat front is faster in experiments than in simulations.

Two experiments were performed at the Omega laser facility[16] of the Laboratory for Laser Energetics (Rochester, NY). The targets were carbon foams of densities ranging from 5 to 50 mg/cm^3, loaded with 2 to 16 atomic % of Cu. To describe the x-ray generation process, we present here absolute x-ray yield measurements, x-ray spectra and time-resolved x-ray imaging.

In section II, we briefly present the targets and their fabrication processes. Section III details the experimental configuration. The experimental results are presented in sections IV, V, VI and VII, along with numerical modeling. Finally, we conclude in section VIII with a discussion of the possible effects of the foam microstructure.

II. C–CU FOAMS

Two new methods to fabricate low-density ($<$ 50 mg/cm^3), high-Cu-concentration foams have been developed in the course of the present study. These methods have produced, to our knowledge, the lowest-density metal nanofoams with no other major constituents present with atomic numbers $Z > 6$.

The first method[17] starts with making carbon-nanotube (CNT) aerogels with a monolith density of $\sim$ 25 mg/cm^3 with a CNT loading of $\sim$ 55 at. % (relative to the carbon binder). The pores of the aerogel monolith are then filled with an aqueous solution of $CuSO_4$, followed by flash-freezing by immersing into liquid nitrogen, freeze-drying (vacuum desiccation) to remove water, and pyrolysis for thermal decomposition of $CuSO_4$. This technique yielded Cu–C composite foams with total monolith densities varying from 30 to 50 mg/cm^3, with 3 to 13 at.% of Cu loading.

The second method[18] starts with a suspension of CNTs and graphene oxide (GO) in an aqueous solution of $CuSO_4$. This solution undergoes a process similar to

[a)] Present Address: LULI, Ecole Polytechnique, 91128 Palaiseau Cedex, France

[b)] Electronic mail: fournier2@llnl.gov

Name	Density	Cu concentration
A28	28 mg/cm^3	4.5 at. %
A42	42 mg/cm^3	2.7 at. %
A43	43 mg/cm^3	10 at. %
A50	50 mg/cm^3	13 at. %
B5	5.1 mg/cm^3	2.5 at. %
B6	6.5 mg/cm^3	8 at. %
B8	8.5 mg/cm^3	14 at. %
B9	9 mg/cm^3	16 at. %

Table I. Types of foams studied here.

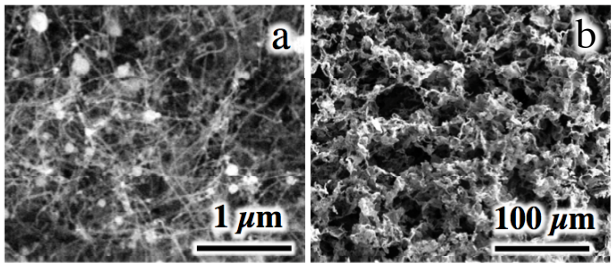

Figure 1. Representative SEM images of Cu–C composites of (a) type A and (b) type B.

the first method: flash-freezing, freeze-drying and pyrolysis. Upon the crystallization of water, the salt and carbon constituents segregate at grain boundaries of water crystallites. The pyrolysis reduces the graphene oxide, leaving a low-density structure of graphitic carbon foam with embedded Cu nano-particles. With this technique, we obtained foams of densities varying from 5 to 10 mg/cm^3, with 2.5 to 16 at. % of Cu loading. Both monolith density and Cu loading are controllable by the choice of CNT, GO, and $CuSO_4$ concentrations in the starting solution[18].

More details on the fabrication and characterization of these foams are available in Refs. 17 and 18. For both methods, the foams contained approximately 1 at. % of Ni as Ni was used as the catalyst for the growth of CNTs. The densities and compositions of the foams that were fielded in this study are listed in Table I. The types A and B refer to the first and second fabrication processes described above, respectively.

Fig. 1 shows scanning electron microscope (SEM) images of these two types of foams, demonstrating their widely different morphologies. Type A presents a sub-micron filamentary structure, while type B has pores of typical sizes of a few tens of microns.

III. EXPERIMENTAL CONFIGURATION

As illustrated in Fig. 2, the foams were held in a polyimide cylinder (2 − 2.2 mm long, 2 mm diameter, 50 μm-thick wall). In a few cases, we attached the foam directly to a glass stalk with a small droplet of glue. The

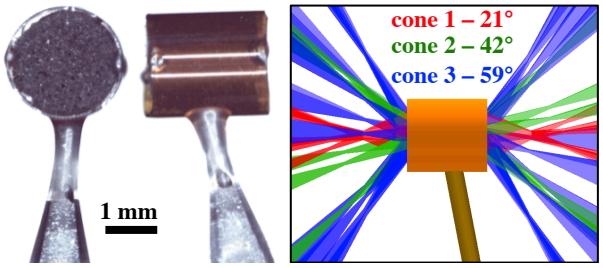

Figure 2. (Color online) Left: photographs of a mounted C/Cu foam target. Right: laser irradiation geometry.

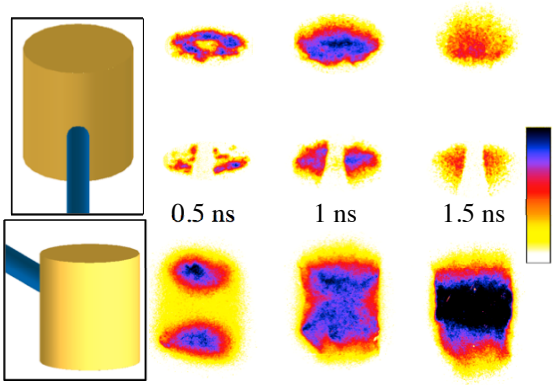

Figure 3. (Color online) Images of the Cu K-shell emission at three different times (±0.2 ns). The top and bottom rows correspond to targets of types A50 and B8, respectively.

two experiments carried out at the Omega laser facility used forty laser beams (twenty on each face of the cylinders). Each beam delivered 500 J, for a total of 20 kJ, in a 1 ns square pulse at a wavelength of 351 nm. The lasers are arranged in three cones of different incident angles, shown in the right panel of Fig. 2. The total irradiation pattern was set to provide an approximately uniform intensity of 10^{15} W/cm^2 on a 1-mm-diameter area. Details regarding the Omega laser, the target chamber, and each diagnostic instrument can be found in the National Laser User Facility User's Guide[19].

IV. GATED X-RAY IMAGES

To provide qualitative insight into the laser plasma interaction and the plasma dynamics involved in these experiments we present, in this section, two-dimensional images of the x-ray emission from the target, acquired using an x-ray framing camera (XRFC)[20]. Twelve pinholes projected the images onto a gated micro-channel-plate detector. It is configured to produce three sequential exposures (each lasting 50 ps), beginning at $t = 0$ ns, 0.5 ns, 1.0 ns, and 1.5 ns (±0.2 ns). Filtering using Al and Be foils eliminated the soft x rays, so that the K-shell emission provided the dominant signal. The XRFC had

a near side-on view of the target in order to investigate the heating pattern along the cylinder axis.

Fig. 3 shows XRFC images from two different targets, A50 and B8. The former is representative of all targets of type A, and the latter is representative of all targets of type B. At early times, the x-ray emission appears mostly close to the faces of the cylinders, and has a tendency to penetrate farther inside the foam as time goes on. However, it is clear that the denser foams (type A, top row in Fig. 3) do not exhibit significant laser penetration, while the low-density foams of type B emit x rays from their entire volume. This observation is consistent with the localized energy deposition in high-density plasmas: comparing the maximum electron density n_e of each target with the critical density[12] $n_c \sim 10^{22}$ cm^{-3}, the type-B targets have n_e between 15 and 30% of n_c while type-A targets have n_e between 90 and 150% of n_c.

V. HEAT FRONT PROPAGATION

An x-ray streak camera 'SSCA' monitored the plasma dynamics in a more quantitative way than XRFC. It consisted of a slit (20 μm-wide, magnification of 10) imaging the target onto a Au photocathode. Another slit, on the photocathode, selected the central region. Streaking this one-dimensional image then provided a temporal resolution < 0.1 ns. X-ray film was used as the detector, and adequate filtering was employed to isolate the emission from the Cu K-shell (7 - 10 keV).

This diagnostic did not capture precise data with targets of type A, because, as already shown in Sec. IV, negligible front propagation was observed in this case. Three examples from type-B targets are shown in the left column of Fig. 4, corresponding to three different foam densities. Early in time, x-ray emission is observed near the edges of the targets (at 0 and 2 mm), corresponding to the faces of the cylinders. At $t = 0.5$ ns, the x-ray emission has progressed towards the center of the target. At $t = 1$ ns, all the target is emitting, but soon after, this emission abruptly stops in most of the plasma, corresponding to the end of the laser pulse.

For the lowest density targets, B5 and B6, the center continues emitting for significant time afterwards. This afterglow results from the overlap of lasers from both sides providing additional heating and compression.

For a quantitative comparison of the heat front velocities between different targets, we define the heat front position to be at half-maximum of the x-ray signal. The front position is plotted as a function of time in Fig. 5 (solid lines), for different foam types. For decreasing foam density, the front appears to advance faster through the foam. We measure its velocity at the middle of the laser pulse ($t = 0.5$ ns) and report these measurements in Fig. 6 as a function of foam density. A clear trend is observed: the velocity decreases as a function of density. This is primarily explained by the inverse Bremsstrahlung absorption being proportional to the square of the electron density, so that denser targets absorb laser light in a shorter distance.

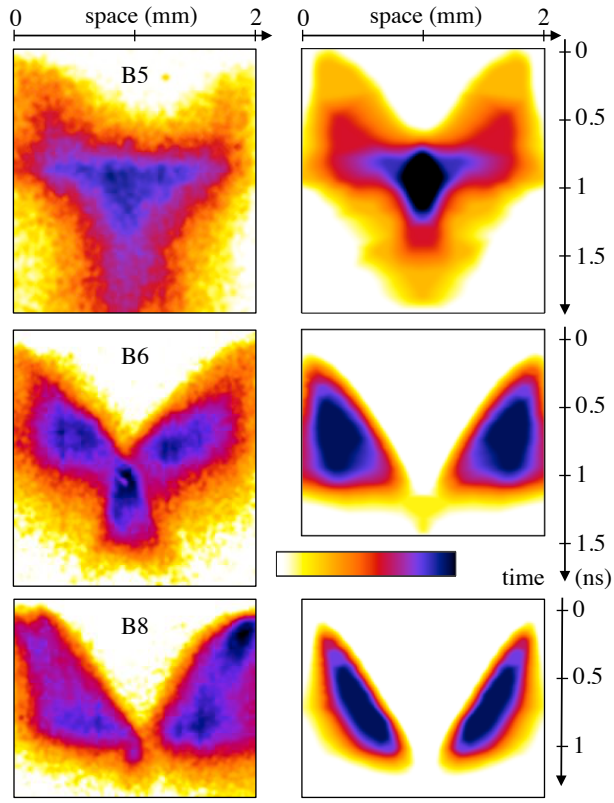

Figure 4. (Color online) Left: time-resolved x-ray images from the SSCA streak camera for targets of types B5, B6 and B8. Right: corresponding images from post-processing LASNEX simulations.

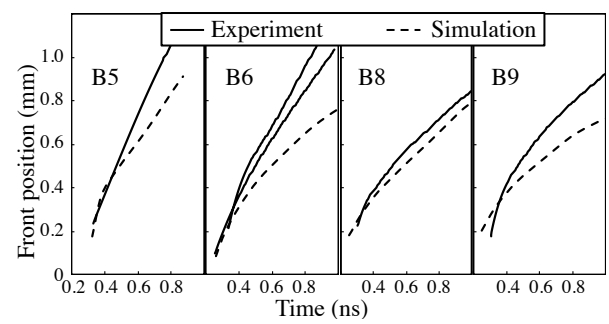

Figure 5. (Color online) Heat front position *vs.* time for different foam types.

To the authors' knowledge, no other front velocity measurements have been reported in the past with similar targets. Instead, silica-based aerogels have been studied thoroughly[13,14,21,22], using Ti or Ge dopants for x-ray emission: velocities of the order of 0.5 to 2 mm/ns have been measured for various geometries, showing similar scaling with foam density as that described here.

The LASNEX radiation-hydrodynamics code[23] was em-

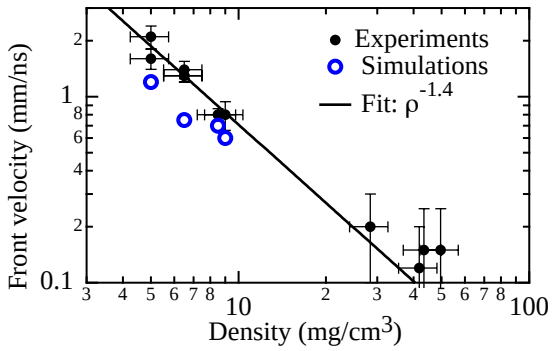

Figure 6. (Color online) Heat front velocity at $t = 0.5$ ns (middle of the laser pulse) from the SSCA experimental data (black dots), from LASNEX simulations (blue circles), and a power-law fit (solid curve)

ployed to simulate the laser-plasma interaction in a cylindrical geometry. It uses a Lagrangian formulation of the equations of motion, with the equation of state given by the non-local thermodynamic equilibrium (non-LTE) rate equations. A super-configuration non-LTE atomic model[24] provides the ionization levels. The ray-tracing laser propagation includes inverse Bremsstrahlung on the free electrons. Electron thermal conduction is treated according to the model described by Schurtz, Nicolaï, and Busquet[25].

Using this LASNEX model, post-shot simulations were performed for each of the target types listed in Table I, using the actual as-measured target dimensions, nominal densities, and the as-measured laser beam energies. The foam is assumed to be homogeneous in the simulations; we have found in separate simulations that include microstructure that the homogenization time (that is, the time for the foam filaments to fill the foam pores or voids) is very short compared to the laser pulse duration, on the order of a few to a few tens of ps, so the assumption of homogeneous foam is reasonable.

The simulations were post-processed to produce simulated streak camera images of the heat-front propagation. Three such simulated images are shown in the right column of Fig. 4. The simulated heat front position as a function of time is compared to the measured ones for the four targets of type B in Fig. 5.

Note that the simulations capture the trend of heat-front velocity decreasing with increasing foam density that is evident in the data, as shown in Fig. 6. The absolute value of the simulated heat-front velocity, while close to the measured value, is lower in all cases. All the foams appear to behave as if they have an effective density that is $\sim 20\%$ less than the nominal density. We discuss this finding in more detail in section VIII, particularly how the unique microstructure of these foams can possibly explain this behavior.

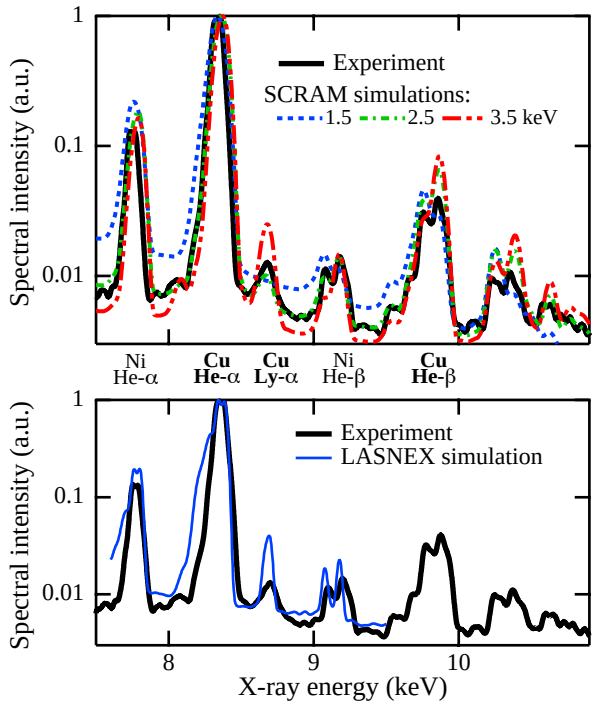

Figure 7. (Color online) Top: time-integrated spectrum of a target of type B6 compared with predictions from the SCRAM code assuming different uniform temperatures. Bottom: same experimental spectrum compared to the corresponding LASNEX simulation.

VI. X-RAY SPECTRA

The HENWAY spectrometer was used to determine the spectral content of the K-shell emission, from 7 to 11 keV approximately. It consisted of a pentaerythritol crystal (interatomic distance $2d = 8.742$ Å) and an x-ray film detector. Filtration with different sets of metallic foils allowed for reconstructing the spectrum over a large dynamic range.

The top panel in Fig. 7 shows an example of an experimental spectrum acquired by HENWAY in the case of a target of type B6. Several line denominations are indicated in the figure. Both Cu and Ni lines are visible in the spectrum, with emphasis of the Cu lines as the Cu is more abundant than the Ni.

The peak-temperature region of the plasma tends to emit more K-shell x rays as long as its density is high. Thus, assuming limited plasma expansion, we can consider that a significant fraction of the K-shell emission originates from regions close to the peak temperature, and we can compare the spectra to single-temperature simulations. We employed the SCRAM[26] code, which produces x-ray spectra given a uniform plasma, self-consistently accounting for absorption of the emitted light. Several cases are plotted in the top panel of Fig. 7, corresponding to plasma temperatures of 1.5, 2.5 and 3.5 keV. Line lev-

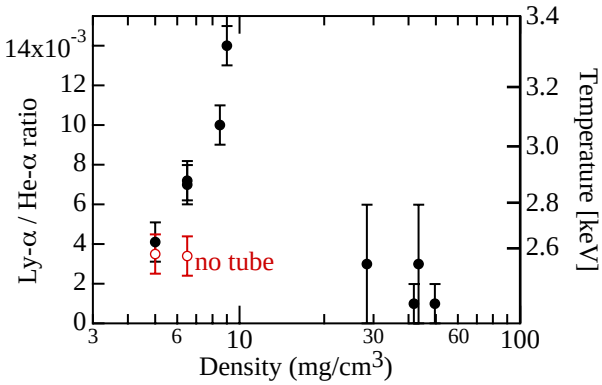

Figure 8. (Color online) Cu Ly-α to He-α lines ratio from the HENWAY spectrometer experimental data. The right-hand-side axis provides equivalent temperatures by comparison to SCRAM simulations.

els and widths are generally in good agreement with the experimental spectrum, especially for a 2.5 keV temperature.

The bottom panel in Fig. 7 compares this same experimental spectrum with the spectrum calculated with the non-LTE detailed atomic model in LASNEX and convolved with the response function of the spectrometer. The agreement is reasonably good. The simulations show the same trend of increasing plasma temperature with density in the foams of Type B, with a peak temperature of 2.9 to 3.6 keV.

The characteristic most sensitive to the plasma temperature is the strength of the Cu Ly-α line compared to that of the He-α line. Indeed, the difference corresponds to one of the remaining K-shell electrons being ionized or not, with a binding energy of ~ 9 keV. This ionization starts occurring around a temperature of 2.5 keV.

For a more quantitative comparison, the ratio of the signals contained in the Cu Ly-α and He-α lines (above continuum emission) has been calculated and plotted in Fig. 8. Concerning targets of type B (density < 10 mg/cm^3), a clear trend is observed, showing an increasing ratio with increasing density. The ratios increase from 0.004 to 0.014, which, according to the SCRAM simulations, corresponds to an increase of temperature from 2.6 to 3.2 keV. This increase in temperature with density is close to what is seen in the LASNEX simulations, as discussed above. These simulations, however, cannot provide accurate line ratios.

The targets of type A do not show such a temperature increase. Due to their low signal, the large error bars indicate that the corresponding temperature is below 2.5 keV, which is close to the detection limit of $\sim 2-2.5$ keV. This low apparent temperature of targets of type A is likely due to their high density: the plasma expansion is significant as the laser cannot penetrate the foam, and we cannot make the assumption that the bulk of the foam emits most of the x rays. The x-ray emission is then likely to originate from a colder, expanded plasma, which agrees with the images presented in section IV.

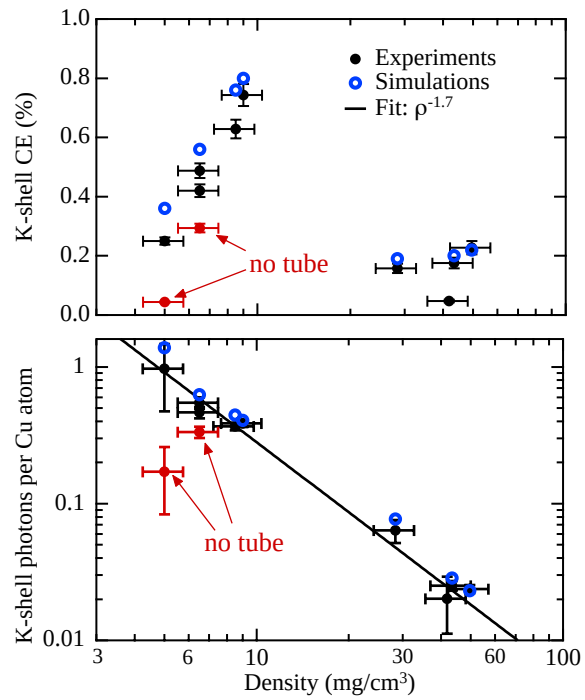

Figure 9. (Color online) K-shell yields *vs.* target density, as measured by DANTE (black dots), as simulated (blue circles) and compared to a power-law fit (black curve). Top: laser-to-K-shell conversion efficiency. Bottom: K-shell photon per Cu atom. Note that the error bars do not account for the possible anisotropy of the x-ray emission.

VII. ABSOLUTE X-RAY YIELDS

To measure the laser-to-x-ray conversion efficiency (CE), the absolute x-ray power from the target was acquired with the DANTE instrument[27]. It consists of 11 time-resolved channels sensitive to different x-ray energies, overall spanning a wide range (60 eV to 10 keV). The detectors are vacuum x-ray diodes with Al, Ni, or Cr cathodes and filtration depending on the energy range to be detected. Time-resolved signals from the diodes are acquired with high-speed (5 GHz) digitizers. DANTE is absolutely calibrated in a synchrotron facility, and absolute x-ray yields can be determined from the waveforms of each channel.

The K-shell (7 to 10 keV) yield measurements are reported in Fig. 9 as a function of target density. Targets mounted directly on a stalk, without a tube holder, are highlighted with red arrows. The laser-to-x-ray conversion efficiency (top panel) indicates a maximum CE of 0.75%, obtained with the 9 mg/cm^3 foams. The CE is consistently below 0.25% for the high-density targets.

This low efficiency is due to the highly localized laser absorption, preventing the laser from heating a large volume, as described in section IV.

The CE also drops quickly on the low-density side but for a different reason: the Cu doping is very low in that limit, thus producing little signal. To account for this varying Cu content, the bottom panel of Fig. 9 shows the number of K-shell photons divided by the total number of Cu atoms in the target. Discarding the targets without a tube holder, the trend shows that the targets of lowest densities make the highest efficiency per Cu atom. Indeed, in section IV, we have shown that these targets are heated over their whole volume, explaining their high efficiency.

VIII. DISCUSSION AND CONCLUSIONS

The ±20% horizontal error bars on the measurement data points in Figs. 6 and 9 represent the measurement uncertainty in the foam density, largely due to the uncertainty in the volume measurement; the foams were not perfect right-circular cylinders, so approximations were made in determining volume from measurements of length and diameter prior to insertion in the polyimide tubes.

Note in Fig. 9 that the simulated K-shell x-ray yields agree with the measured yields to within the measurement uncertainty of the density. The discrepancy between simulations and data, however, is in one direction only; that is, the foams behaved as if all of them were at $\sim 20\%$ lower density than nominal, which is the same discrepancy as for the heat-front propagation velocity discussed in Section V. Thus, the discrepancy cannot be explained by the density measurement uncertainty, since the measurement uncertainty would be expected to lead to a random offset between simulation and measurement, not a systematic offset.

Since both the measured K-shell yield and heat-front propagation velocity come from the Cu nanoparticles embedded in the C foam, we must consider how the Cu is distributed in the C foam matrix. We see that the nanoparticles are fairly uniformly distributed in the foam, at all length scales (see the SEM images in Fig. 5 of Ref. 18). The nanoparticles are close-to-spherical in shape, but they have a distribution of sizes, as shown in Fig. 6 of Ref. 18. Most of the nanoparticles have a diameter of a few tens of nanometers or less, comparable to a few skin depths of the laser light in solid Cu. Accordingly, we can assume that the entire volume of these smaller nanoparticles becomes homogenized plasma when illuminated by the laser light. Approximately one quarter of the nanoparticles, however, have a larger diameter than the average, with the largest nanoparticles having a diameter about twice the average. Thus, a larger fraction of the overall mass of the foam is contained in these larger-than-average nanoparticles.

If we assume that only the outer layers of the more massive nanoparticles, down to a few skin depths, contribute Cu atoms to the homogenized and ionized plasma, then we can define an overall *effective* density for the homogenized plasma that is up to $\sim$ 20-25% less than the nominal (un-ionized) density of the foam. With this definition of effective density, we find very good agreement of the non-LTE atomic model simulations with data.

There could, of course, be some other explanation for the systematic offset between simulation and data. We are pursuing additional experiments to test approximations made in the simulations, including the flux-limited and non-local electron thermal conduction. Furthermore, there may be other effects of the microstructure that are responsible. Experiments comparing gas targets with foam targets that have identical densities and charge states, which we are planning for the future, may lead to more definitive conclusions.

In the meantime, we conclude that the microstructure, in general, likely plays a role in determining how laser light heats foam and propagates within. The unique microstructure of these C-Cu foams may explain differences observed with other foam types.

ACKNOWLEDGMENTS

This work was performed under the auspices of the U.S. Department of Energy by Lawrence Livermore National Laboratory under contract DE-AC52-07NA27344, with partial support from the DTRA Basic Research grant #BRCALL08-PR3-C-2-0006.

REFERENCES

[1] L. Willingale, S. R. Nagel, A. G. R. Thomas, C. Bellei, R. J. Clarke, A. E. Dangor, R. Heathcote, M. C. Kaluza, C. Kamperidis, S. Kneip, K. Krushelnick, N. Lopes, S. P. D. Mangles, W. Nazarov, P. M. Nilson, and Z. Najmudin, Phys. Rev. Lett. **102**, 125002 (2009).

[2] M. A. Purvis, V. N. Shlyaptsev, R. Hollinger, C. Bargsten, A. Pukhov, A. Prieto, Y. Wang, B. M. Luther, L. Yin, S. Wang, and J. J. Rocca, Nat. Photon. **7**, 796 (2013).

[3] P. E. Young, M. D. Rosen, J. H. Hammer, W. S. Hsing, S. G. Glendinning, R. E. Turner, R. Kirkwood, J. Schein, C. Sorce, J. H. Satcher, A. Hamza, R. A. Reibold, R. Hibbard, O. Landen, A. Reighard, S. McAlpin, M. Stevenson, and B. Thomas, Phys. Rev. Lett. **101**, 035001 (2008).

[4] K. B. Fournier, C. Constantin, J. Poco, M. C. Miller, C. A. Back, L. J. Suter, J. Satcher, J. Davis, and J. Grun, Phys. Rev. Lett. **92**, 165005 (2004).

[5] K. B. Fournier, J. H. Satcher, M. J. May, J. F. Poco, C. M. Sorce, J. D. Colvin, S. B. Hansen, S. A. MacLaren, S. J. Moon, J. F. Davis, F. Girard, B. Villette, M. Primout, D. Babonneau, C. A. Coverdale, and D. E. Beutler, Phys. Plasmas **16**, 052703 (2009).

[6] F. Pérez, J. J. Kay, J. R. Patterson, J. Kane, B. Villette, F. Girard, C. Reverdin, M. May, J. Emig, C. Sorce, J. Colvin, S. Gammon, J. Jaquez, J. H. Satcher, and K. B. Fournier, Phys. Plasmas **19**, 083101 (2012).

[7] J. Workman and G. A. Kyrala, Rev. Sci. Instrum. **72**, 678 (2001).

[8] D. Babonneau, M. Primout, F. Girard, J. P. Jadaud, M. Naudy, B. Villette, S. Depierreux, C. Blancard, G. Faussurier, K. B.

Fournier, L. Suter, R. Kauffman, S. Glenzer, M. C. Miller, J. Grün, and J. Davis, Phys. Plasmas **15**, 092702 (2008).
[9]C. A. Back, J. Grun, C. Decker, L. J. Suter, J. Davis, O. L. Landen, R. Wallace, W. W. Hsing, J. M. Laming, U. Feldman, M. C. Miller, and C. Wuest, Phys. Rev. Lett. **87**, 275003 (2001).
[10]K. B. Fournier, M. J. May, J. D. Colvin, J. O. Kane, M. Schneider, E. Dewald, C. A. Thomas, S. Compton, R. E. Marrs, J. Moody, E. Bond, P. Michel, J. H. Fisher, C. D. Newlander, and J. F. Davis, Phys. Plasmas **17**, 082701 (2010).
[11]K. B. Fournier, M. J. May, J. D. Colvin, M. A. Barrios, J. R. Patterson, and S. P. Regan, Phys. Rev. E **88**, 033104 (2013).
[12]W. L. Kruer, *The physics of laser plasma interactions* (Westview Press, 2003).
[13]M. Primout, D. Babonneau, L. Jacquet, B. Villette, F. Girard, D. Brebion, P. Stemmler, K. Fournier, R. Marrs, M. May, R. Heeter, R. Wallace, H. Nishimura, S. Fujioka, M. Tanabe, and H. Nagai, High Energy Density Phys. **9**, 750 (2013).
[14]F. Pérez, J. R. Patterson, M. May, J. D. Colvin, M. M. Biener, A. Wittstock, S. O. Kucheyev, S. Charnvanichborikarn, J. H. S. Jr, S. A. Gammon, J. F. Poco, S. Fujioka, Z. Zhang, K. Ishihara, N. Tanaka, T. Ikenouchi, H. Nishimura, and K. B. Fournier, Phys. Plasmas **21**, 023102 (2014).
[15]P. Nicolaï, M. Olazabal-Loumé, S. Fujioka, A. Sunahara, N. Borisenko, S. Gus'kov, A. Orekov, M. Grech, G. Riazuelo, C. Labaune, J. Velechowski, and V. Tikhonchuk, Phys. Plasmas **19**, 113105 (2012).
[16]T. Boehly, Opt. Commun. **133**, 495 (1997).
[17]S. Charnvanichborikarn, S. J. Shin, M. A. Worsley, I. C. Tran, T. M. Willey, T. v. Buuren, T. E. Felter, J. D. Colvin, and S. O. Kucheyev, J. Mater. Chem. A **2**, 962 (2013).
[18]S. Charnvanichborikarn, M. A. Worsley, M. Bagge-Hansen, J. D. Colvin, T. E. Felter, and S. O. Kucheyev, J. Mater. Chem. A **2**, 18600 (2014).
[19]*National Laser User Facility User's Guide*, University of Rochester, Laboratory for Laser Energetics, Rochester, NY (2007).
[20]D. K. Bradley, P. M. Bell, J. D. Kilkenny, R. Hanks, O. Landen, P. A. Jaanimagi, P. W. McKenty, and C. P. Verdon, Rev. Sci. Instrum. **63**, 4813 (1992).
[21]M. Tanabe, H. Nishimura, N. Ohnishi, K. B. Fournier, S. Fujioka, A. Iwamae, S. B. Hansen, K. Nagai, F. Girard, M. Primout, B. Villette, D. Brebion, and K. Mima, High Energy Density Phys. **6**, 89 (2010).
[22]C. Constantin, C. A. Back, K. B. Fournier, G. Gregori, O. L. Landen, S. H. Glenzer, E. L. Dewald, and M. C. Miller, Phys. Plasmas **12**, 063104 (2005).
[23]J. A. Harte, W. E. Alley, D. S. Bailey, J. L. Eddleman, and G. B. Zimmerman, ICF Quarterly Report, July-September 1996, Volume 6, Number 4, Lawrence Livermore National Laboratory, document no. UCRL-LR-105821-96-4.
[24]H. Scott and S. Hansen, High Energy Density Phys. **6**, 39 (2010).
[25]G. P. Schurtz, P. D. Nicolaï, and M. Busquet, Phys. Plasmas **7**, 4238 (2000).
[26]S. Hansen, J. Bauche, C. Bauche-Arnoult, and M. Gu, High Energy Density Phys. **3**, 109 (2007).
[27]H. N. Kornblum, R. L. Kauffman, and J. A. Smith, Rev. Sci. Instrum. **57**, 2179 (1986).